Dynamic load and stress analysis of a large Horizontal Axis Wind Turbine using full scale fluid-structure interaction simulation

AUTHORS: G. Santo[a*], M. Peeters[b], W. Van Paepegem[b], J. Degroote[a,c]

[a] Department of Flow, Heat and Combustion Mechanics, Ghent University

Sint-Pietersnieuwstraat 41 – 9000 Ghent, Belgium

{gilberto.santo; joris.degroote}@ugent.be

[b] Department of Materials, Textiles and Chemical Engineering, Ghent University

Technologiepark-Zwijnaarde 907 - 9052 Zwijnaarde, Belgium

{mathijs.peeters; wim.vanpaepegem}@ugent.be

[c] Flanders Make, Belgium

[*] corresponding author

Keywords: *Fluid-structure interaction, wind turbine, atmospheric boundary layer, composite materials, wind energy*

ABSTRACT.

A dynamic load and stress analysis of a wind turbine is carried out using transient fluid-structure interaction simulations. On the structural side, the three 50 m long commercial glass-fiber epoxy blades are modelled using shell elements, accurately including the properties of the composite materials. On the fluid side, a hexahedral mesh is obtained for every blade and for the hub of the machine. These meshes are then overlaid to a structured background mesh through an overset technique. The displacements prescribed by the structural solver are imposed on top of the rigid rotation of the turbine. The atmospheric boundary layer (ABL) is included using the k-epsilon turbulence model. The computational fluid dynamics (CFD) and computational solid mechanics (CSM) solvers are strongly coupled using an in-house code. The transient evolution of loads, stresses and displacements on each blade is monitored throughout the simulated time. The ABL induces oscillating axial displacements in the outboard region of the blade. Furthermore, the influence of gravity on the structure is accounted for and investigated, showing that it largely affects the tangential displacement of the blade. The oscillating deformations lead to sensible differences in the torque provided by each blade during its rotation.

1. INTRODUCTION

The last decades have been characterized by a large increase in the interest of academia and industry in wind energy conversion systems all over the world. Despite the fact that these systems have been used since the ancient times, a big impulse to their development was transmitted by the objectives that both EU and US established regarding the increase of the portion of electricity coming from renewable energy sources. The EU members agreed about a program of investments (Horizon 2020) which aims to raise the percentage of electricity from renewable and sustainable sources to 20% by 2020. Simultaneously, the US Government established the objective that 25% of their energy demand should be supplied by wind power by 2025. As a result, the research about wind energy conversion systems has experienced a noticeable boost. Part of this research is currently focused on the simulation of fluid-structure interaction (FSI) of wind turbines.

With the growing dimensions of the rotor of a horizontal axis wind turbine [1] and the increasing slenderness of the blades, their deflection due to the wind load can reach peaks of 10-15% of the total span [2, 3]. As a consequence, the deformed shape of the blades influences the wind flow around them, which in turn affects the structural deflection. This results in a fully coupled problem which is important to take into account in several processes such as the design, the maintenance estimation and the aerodynamic behavior assessment of large horizontal axis wind turbines (HAWTs) [4].

Both the aerodynamic and the structural sides of the FSI problem involve a large number of complexities when it comes to numerical simulation. On the aerodynamic side, the high Reynolds number of the flow (up to 10^8) and the consequent high turbulence levels are challenging to simulate. The rotation of the blades makes the problem even harder to tackle. Furthermore, wind turbines are immersed in the atmospheric boundary layer (ABL), i.e. an increasing wind speed with height, such that the complete rotor has to be simulated with the loads on each blade fluctuating in time. On the structural side, HAWT blades are normally made of anisotropic composite materials built up of several plies. The presence of inner structures (shear webs and shear caps) and adhesive joints makes the modelling even more challenging.

Many works have been carried out involving FSI of wind turbines, ranging a wide spectrum of applications and focuses. MacPhee et al. [5] performed 2D computational fluid dynamics (CFD) simulations of a vertical axis wind turbine (VAWT), using the k-ω-SST turbulence model. This methodology was coupled with structural simulations based on linear, elastic and isotropic material theory. Kim et al. [6] employed an unsteady vortex lattice method, completed with airfoil experimental data, to compute the wind loads on a 46m long blade and transfer them to a structural model based on non-linear beam composite theory. The results of such an FSI simulation were used for acoustic analysis in the surroundings of the turbine. Lee et al. [7] adopted a full scale model on the structural side of the FSI problem, accurately modelling its inner structures and its composite layering by means of a commercial code (Abaqus). On the fluid side, the loads were computed using Blade Element Momentum (BEM) theory. The BEM theory is widely used in FSI simulations of wind turbines [19, 20, 21]. Heinz et al. [8] developed an in-house code capable of loosely coupling BEM or CFD calculations with a structural model employing beams and punctual bodies. Several operating conditions were simulated in this way, ranging from emergency shutdown to regular pitching movements.

On the fluid side, the fidelity has also been increased compared to BEM theory. Yu et al. [18] coupled Reynolds Averaged Navier-Stokes (RANS) simulations with a structural model based on non-linear beam theory and were able to simulate several conditions. Bazilevs et al [2, 3, 9, 10] coupled a more complete structural model with CFD simulations featuring a variational multi-scale turbulence model. The whole analysis is carried out in an isogeometric environment. On the structure side, a full model of the turbine blade is built employing composite layups with constant thickness plies and additional strips of material in order to realistically predict the stiffness of the structure. Despite the high level of detail provided by the latter works, the effect of the ABL is neglected. Furthermore, the computational power necessary to perform these simulations is high due to the necessary grid and time resolution.

The present work aims at simulating the dynamic, fully coupled FSI problem on a full scale HAWT, with a diameter of 100m, employing high-fidelity flow and structural models, leading to a fully coupled FSI model. Unlike in prior literature, the ABL is taken into account in detail. On the structural side, a complete and accurate model reproducing the complex composite nature of each blade is built and employed. The implicit coupling between the flow and the structural models is guaranteed by the in-house code Tango, resulting in a segregated approach [11]. The observed oscillating loads and stresses on each blade are analyzed in depth and the resulting deformations are correlated to the changes in the energy conversion performance of each blade, which is novel compared to the available literature.

First, the details of the CFD model are given in section 2, then the full-scale structural model of the employed blade in section 3. Subsequently, characteristics of the coupling strategy are given in section 4 and, finally, the results are presented in section 5, before drawing the conclusions.

2. THE CFD MODEL

In terms of modelling, the inclusion of the ABL implies that the entire rotor needs to be analyzed and the reduction to one single blade with periodic boundary conditions is not possible. The layout of the complete CFD model is shown in fig. 1.

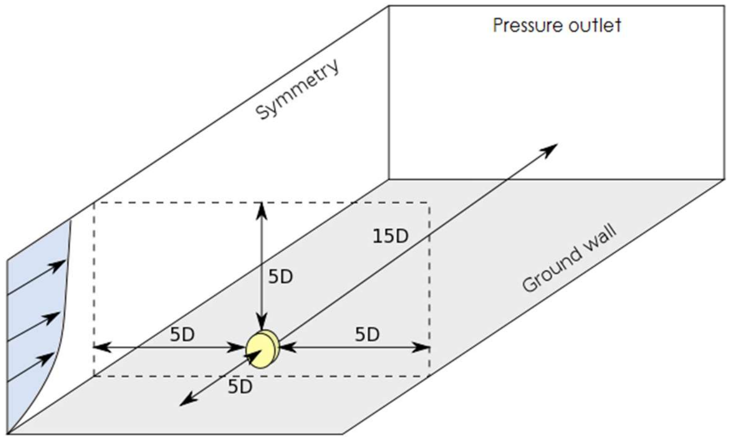

Fig. 1 – Layout of the HAWT simulations (fluid side).

The distance of the rotor from the symmetry sides and top surface (fig. 1) is chosen equal to 5 rotor diameters in order to avoid artificial acceleration of the flow. The inlet and the outlet (atmospheric pressure outlet) are respectively 5 and 15 rotor diameters away from the rotor. These distances are chosen sufficiently large to avoid any influence of the boundaries on the flow around the turbine, as prescribed by best practice guidelines for atmospheric flows [22]. Nevertheless, many works (e.g. [2, 3, 9]) adopt much smaller boundary distances.

A 3D mesh is created for every object to be simulated (namely the hub, and the three blades, fig. 2 - left) and a background structured grid is generated (fig. 2 - right). All these meshes mutually overlay and are connected by an overset technique. Similar techniques have already been used in the aerodynamic side of FSI models of wind turbines [18, 23, 24] with good results. Details of the mesh (C grid) around each blade are shown in fig. 3. The mesh on each wall of the rotor is designed choosing a y^+ in the log layer (between 30 and 300).

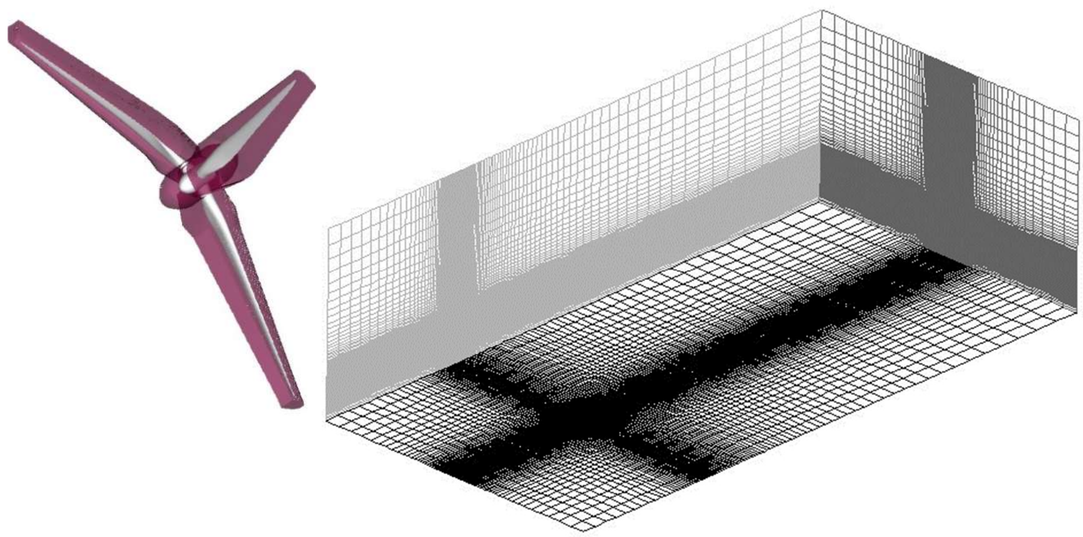

Fig. 2 – (left) component bodies with overset boundaries (in red) and (right) background structured mesh.

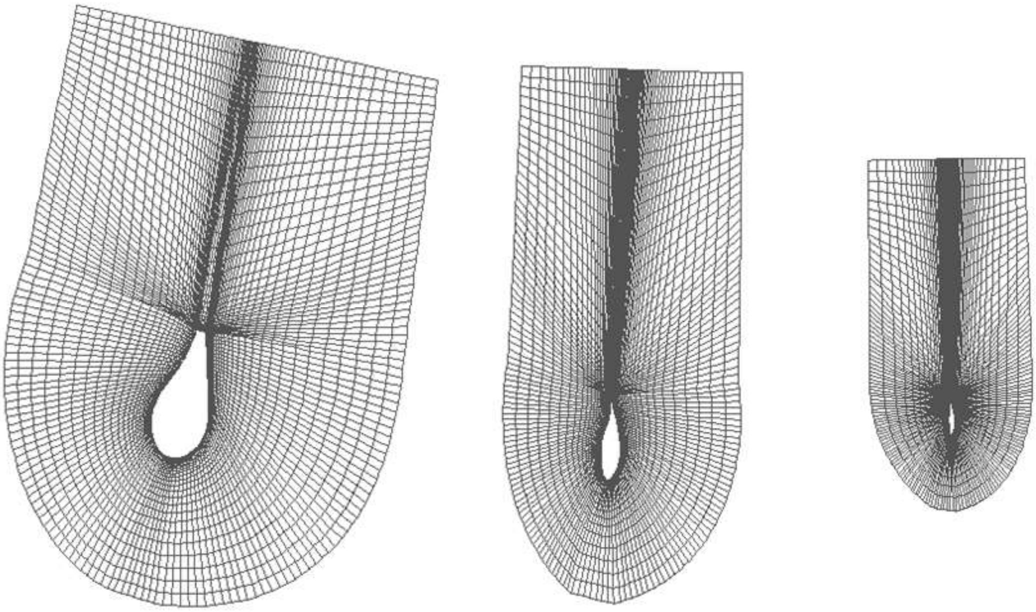

Fig. 3 – Sections of the fluid component mesh around a blade: (left) 20% span, (middle) 50% span, (right) 90% span.

As an example of how the mesh connectivity is built, we show the connection of the blade mesh with the background grid. The background cells encompassed or crossed by the blade walls are deactivated. Then, on the external boundary of the component mesh, the solution is obtained by interpolation from the background mesh. Here, the two meshes are designed to have roughly the same cell size. The (background) cells from where the solution is taken are marked as "donor cells", while the (component) cells receiving solution by interpolation are marked as "receptor cells". At least 4 donor cells contribute to interpolation on each receptor cell. This is summarized by fig. 4:

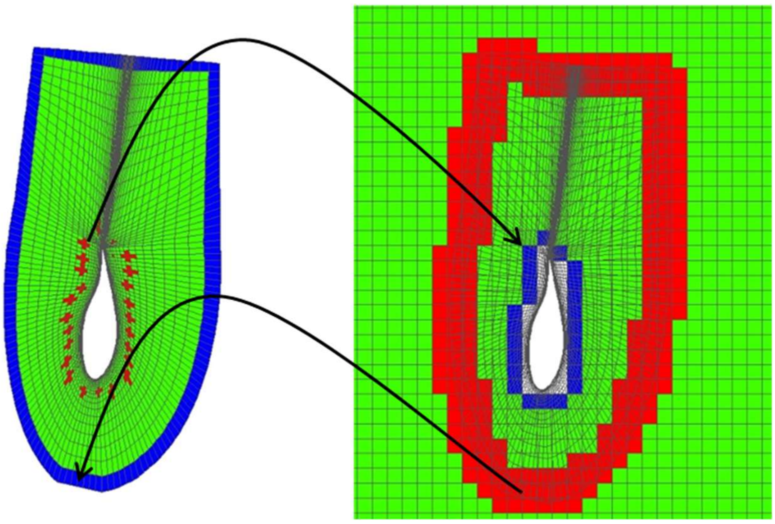

Fig.4 – Mesh connectivity technique: (left) component mesh, (right) background and component mesh overlapped. Solve cells are marked in green, donor cells in red and receptor cells in blue.

The background cells confined between the donor boundary and the blade walls are solved in order to guarantee a buffer of (future donor) cells with valid solution data when the component mesh is moved due to the rotation (fig. 5) or deflection of the blades. As shown in fig. 4, the inner boundary of the background mesh is represented by a border of receptor cells where solution is taken by interpolation from the closest donor cells on the component mesh.

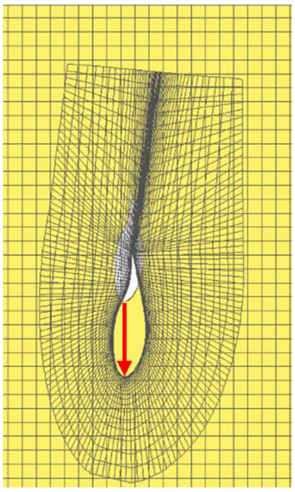

Fig. 5 – Blade component mesh movement due to blade rigid rotation. In yellow, the region of the background mesh where solution is available from previous time step.

The case is considered to be incompressible, given the low Mach numbers typical of the HAWTs. The turbulence model is chosen to be the k-epsilon (unsteady RANS) model for two reasons. First, for this turbulence model, ABL inlet conditions have been obtained by Richard and Hoxey [12] (also used in other works about CFD analysis of wind turbines [25]). Second, extensive work to preserve their stability in the numerical domain has been performed by Parente et al. [14, 15]. The present work relies on the previous work just outlined, which will be now described more in detail.

The k-epsilon model adds the following transport equations to the momentum and continuity equations.

$$\frac{\partial}{\partial t}(\rho k) + \frac{\partial}{\partial x_i}(\rho k u_i) = \frac{\partial}{\partial x_j}\left[\left(\mu + \frac{\mu_t}{\sigma_k}\right)\frac{\partial k}{\partial x_j}\right] + 2\mu_t S^2 - \rho\varepsilon \tag{1}$$

$$\frac{\partial}{\partial t}(\rho \varepsilon) + \frac{\partial}{\partial x_i}(\rho \varepsilon u_i) = \frac{\partial}{\partial x_j}\left[\left(\mu + \frac{\mu_t}{\sigma_\varepsilon}\right)\frac{\partial \varepsilon}{\partial x_j}\right] + C_{1\varepsilon}\frac{\varepsilon}{k}(2\mu_t S^2) - C_{2\varepsilon}\rho\frac{\varepsilon^2}{k} \tag{2}$$

k and ε are respectively the turbulent kinetic energy and its dissipation rate, S represents the modulus of the rate-of-strain tensor and σ_k, σ_ϵ, $C_{1\varepsilon}$ and $C_{2\varepsilon}$ are constants respectively set equal to 1, 1.3, 1.44 and 1.92. The turbulent viscosity μ_t is defined as $\mu_t = C_\mu \rho \frac{k^2}{\varepsilon}$ with C_μ equal to 0.09.

The ABL inlet conditions first proposed by Richard and Hoxey [12] are employed in order to replicate the neutral ABL conditions in the numerical domain, with z the height, thus the distance from the ground wall.

$$u(z) = \frac{u_*}{\mathrm{K}} ln\left(\frac{z + z_0}{z_0}\right) \tag{3}$$

$$k = \frac{u_*^2}{\sqrt{C_\mu}} \tag{4}$$

$$\varepsilon(z) = \frac{u_*^3}{\mathrm{K}(z+z_0)} \quad (5)$$

In these equations, u_* is the friction velocity, an index of the global wind intensity, and z_0 is the aerodynamic roughness length which provides a measure of how rough the ground wall is. These two parameters fully define the ABL characteristics. K is the von Karman constant (0.4187). It can be easily verified that these profiles are an analytical solution of the k-epsilon equations reported above.

To guarantee that the profiles imposed as inlet conditions are preserved throughout an empty domain, a new formulation of the wall functions for the ground wall is required, as observed by Blocken et al. [13] and Parente et al. [14]. Thus, the aerodynamic roughness length is explicitly included in the wall functions, following the formulation proposed by Parente et al. [15], leading to a modified non-dimensional wall distance z^+ and a modified wall function constant E.

$$z^+_{mod} = \frac{(z+z_0)u_*\rho}{\mu} \quad (6)$$

$$E_{mod} = \frac{\mu}{\rho z_0 u_*} \quad (7)$$

In the remainder of this work, the resulting novel wall functions [15] are addressed as “modified wall functions”, in contrast with the standard ones. To validate the ABL modelling approach outlined above, two test cases are described in the appendix, together with their results. The authors who first proposed this approach have also performed extensive validation work [14, 15].

On the inlet surface, the previously defined inlet ABL profiles are prescribed. All the simulations are carried out at the nominal operating point, as declared by the manufacturer of the blades. This point corresponds to a wind speed of 8.5 m/s and a rotational speed of 1.445 rad/s, resulting in a tip speed ratio (TSR) of 8.5. In order to reach 8.5 m/s at the hub height (100 m), in the ABL profiles the friction velocity is set to u_*= 0.671082 m/s and the aerodynamic roughness length is set to z_0= 0.5 m. The value of the aerodynamic roughness length is chosen according to the classification proposed by Davenpoort and Wieringa [26] (corresponding to rough, cultivated landscape in the proximity of the simulated turbine) in order to produce a sheared velocity profile, whose effect can be clearly addressed in the loads and performance of each blade during its rotation. The turbulent kinetic energy is set to $0.01512 m^2/s^2$, producing a turbulent intensity of approximately 1.3% at the hub height (similar to the values used in other CFD simulations of HAWTs [27]). There is no tilt or yaw of the rotor with respect to the incoming wind, which is perfectly aligned with the axis of rotation of the machine. The standard wall functions are employed on the rotor walls, while the modified ones are employed on the ground wall. The momentum equations and continuity equation are solved together in a pressure-based solver. 2nd order upwind discretization for momentum is applied and a 1st order implicit scheme is used for time discretization. The same settings are used for every simulation carried out in this work. The CFD setup is implemented in Fluent 18.1 (Ansys Inc.).

A mesh and time-step independency study was carried out in order to assess the validity of the proposed methodology by comparing the obtained power output with the nominal torque coefficient provided (0.0556) by the manufacturer of the blades. The undisturbed ABL flow is imposed everywhere in the domain and the rotation of the turbine is started. 7 complete revolutions are covered by the simulation time and carried out on 3 different sets of meshes (table 1) and 3 different time-step sizes.

Mesh name	Number of cells	Faces/blade

	Background mesh	Blade mesh	TOTAL	
Coarse	21.68 M	0.76 M	24 M	13380
Medium	49.6 M	1.87 M	55 M	38489
Fine	73 M	2.5 M	80 M	55535

Table 1 – Independency study: details of the used mesh sets.

The torque coefficient (defined in the "results" paragraph) is monitored during the simulation time and Table 2 summarizes the average over the last performed revolution, showing the percentage differences of each setup with respect to the combination of medium mesh and 240 time steps per revolution, which was chosen to be used in the FSI and CFD simulations. For each simulation, the difference in average torque between the last 2 revolutions is smaller than 2%.

Mesh name	**120 time steps / rev** $\Delta t = \mathbf{0.036235}$ **s**	**240 time steps / rev** $\Delta t = \mathbf{0.0181176}$ **s**	**360 time steps / rev** $\Delta t = \mathbf{0.0120784}$ **s**
Coarse	0.04788 (-8.68 %)	0.04925 (-6.06 %)	0.05008 (-4.48 %)
Medium	0.05093 (-2.85 %)	0.05243 (/)	0.05332 (+1.70 %)
Fine	0.0522 (-0.39 %)	0.05356 (+2.16 %)	0.05439 (+3.75 %)

Table 2 – Independency study: torque coefficient averaged over the last revolution for every setup.

Comparing the torque coefficient provided by the manufacturer of the blades and the results obtained for 240 time steps/revolution and medium mesh, as used in all further simulations, a deviation of less than 5.8% is observed.

3. THE STRUCTURAL MODEL

The analyzed blade is entirely made of composite material, with a total mass of 9.42 tons. Several airfoils are lofted throughout its 50 m span. Inside the structure itself, three shear webs cover a large portion of the total span and provide additional stiffness to the blade.

Only shell elements with 3 or 4 nodes and reduced integration are employed and composite layups are defined to reproduce the composite layering in every shell. The elements are positioned on the outer mold layer (OML) with material offset towards the inside, mimicking the blades manufacturing process and maintaining the correct outer blade shape. Different layups are assigned to different regions of the structure, modelling its real composition. A local reference frame is discretely defined in every element in order to fix the global orientation of the layup. Every layup is then composed of a varying number of plies ranging from 1 to 127. For each ply a material and a thickness are assigned, together with a relative orientation in the form of a rotation angle with respect to the global layup orientation. This relative orientation is necessary to fully define the characteristics of layers made of anisotropic materials. In every element, the stresses are computed in each ply. The shear webs and the shear caps are modelled using the same strategy. The adhesive joints are also included in the model by the introduction of layers of adhesive material. The mesh is created according to the process outlined and discussed in [17]. Following this procedure, a mesh composed of 64000 three-dimensional shell elements is obtained, as shown in fig. 6.

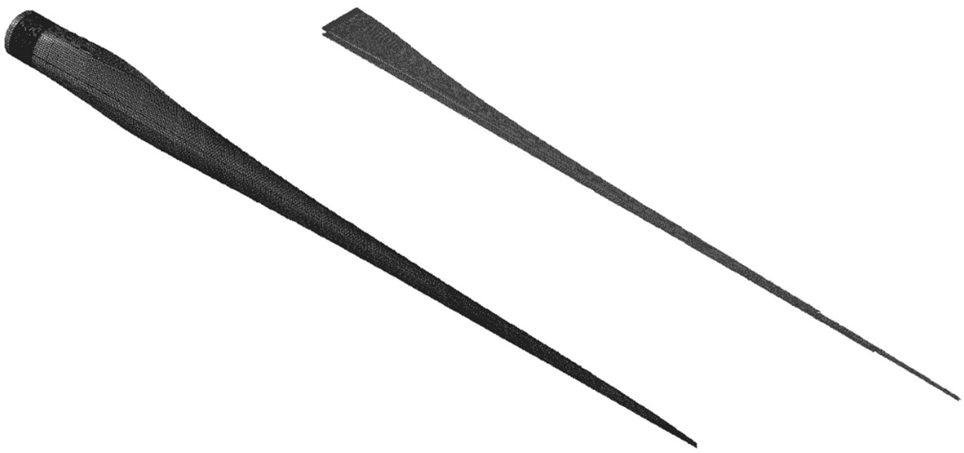

Fig. 6 – Overview of the structural mesh: (left) outer and (right) inner structures.

In order to validate the structural model, the eigenfrequencies of the blade are computed, pinning its root. The manufacturer provides only ranges for the first flap-wise and chord-wise modes as benchmarks. The results of the modal analysis are reported in Table 1.

	Manufacturer	Modal analysis
First flap-wise mode	0.74 Hz - 0.91 Hz	0.645 Hz
First chord-wise mode	1.01 Hz - 1.35 Hz	1.165 Hz

Table 1 – Experimental/numerical comparison of the eigenfrequencies of the blade

In the FSI simulations, the rotational speed around the turbine shaft is fixed at the root of the blade, where any other degree of freedom is constrained.

4. FSI COUPLING

The two outlined models are coupled by an in-house code, named Tango [11]. Within every time step, the information is exchanged as outlined in fig. 7.

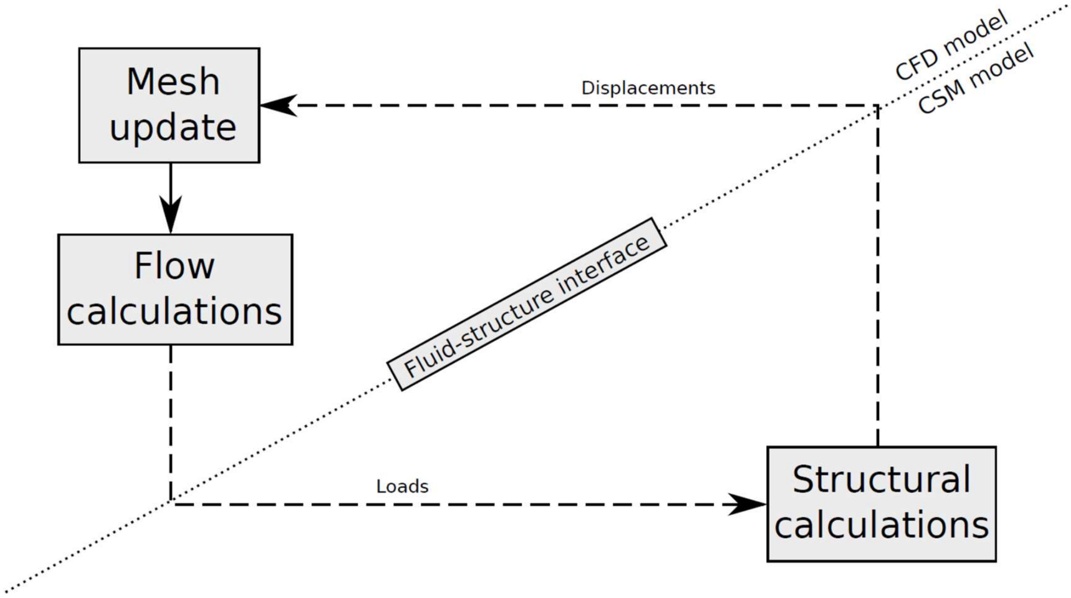

Fig. 7 – FSI coupling scheme for one time step.

This strategy corresponds to the Gauss-Seidel coupling algorithm. Given the non-conformal meshes, interpolation is required when any information (loads or displacements) is passed from one side of the fluid-structure interface to the other. When transferring the fluid loads to the structural mesh, a barycentric interpolation among the 3 nearest points is applied, whereas, when the displacements are to be imposed on the fluid mesh, a local radial basis function interpolation is carried out using the 81 nearest points. At the beginning of every time step, the component meshes in the CFD model (namely the 3 blades and the hub) are rigidly rotated according to the time step size and the chosen rotational speed. In the first coupling iteration of every time step, no mesh update in addition to rigid rotation is performed since there is still no structural data available for the current time step. In subsequent coupling iterations, in addition to the rigid body rotation, the displacements prescribed by the structural solver are applied on the blades at the beginning of every coupling iteration. An arbitrary Lagrangian Eulerian (ALE) formulation is employed for the mesh update. A spring-based method is selected to displace the entire blade component mesh according to the deflection prescribed by the structural solver on the blade wall. Subsequently, the mesh connectivity is re-built before proceeding with the flow calculation. This guarantees a consistent good mesh quality throughout the entire simulation time.

The loop shown in fig. 7 is repeated 3 times within every time step, leading to fluid-structure interface displacement absolute residual to drop to the order of magnitude of 0.003 m. The time step size is chosen according to the output of the sensitivity study reported in section 2 (0.0181176 s). Running on 280 cores (10 nodes, each with 2 CPUs of the type 14-core Xeon E5-2680v4, 2.4GHz, inter-connected via InfiniBand), less than one day is necessary to perform a complete revolution in the CFD case, compared to 1.5 weeks needed in the case of a fully coupled FSI simulation.

5. RESULTS AND DISCUSSION

In this section, the results of different simulations are analyzed. A simulation with rigid blades is compared to a fully coupled FSI simulation. Finally, the effect of the gravity load on the blades is briefly highlighted by comparing the fully coupled FSI simulation with an analogous one carried out neglecting gravity in the structural model ("g-less"). In the remainder, the logics illustrated in fig. 8 will be followed when defining the azimuth angle of each blade and the sign of the radial and tangential forces, velocities and displacements.

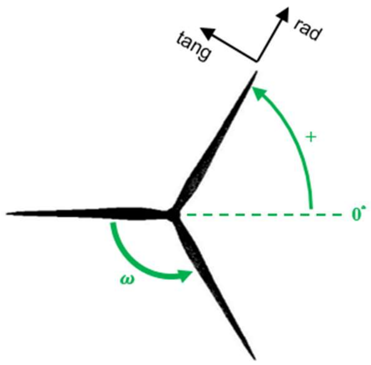

Fig. 8 – Definitions of blade azimuth angle and components of forces and velocities.

Furthermore, as usually done, the torque (T) and the forces (F) acting on the blades are made non-dimensional by means of the following formula:

$$c_T = \frac{T}{\frac{1}{2}\rho v^2 AR} \tag{8}$$

$$c_F = \frac{F}{\frac{1}{2}\rho v^2 A} \tag{9}$$

where ρ is the air density (1.225 kg/m^3), A the frontal area of the rotor and R its radius. The velocity v of the undisturbed flow is chosen to be the wind free stream velocity at the hub height, namely 8.5 m/s.

The FSI simulations are started from the results of a transient simulation with rigid blades, running for a time covering 5 complete revolutions and starting from stand still in the undisturbed ABL. The wind loads acting on the blades at this time instant are used in structural steady state simulations in order to deflect the blades and consistently deform the mesh in the fluid model. Then, 2 more revolutions are carried out with flexible blades. Fig. 9 shows the total torque provided by the turbine during the 2 revolutions performed in the flexible blade simulation.

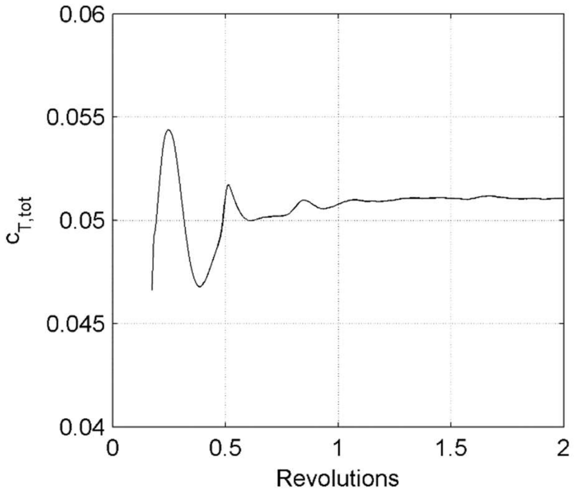

Fig. 9 – Total torque coefficient during the 2 revolutions in FSI mode.

The first revolution is interpreted as necessary to cancel out the influence of the initial solution and reach a periodic regime in time and, for this reason, is not investigated any further. During the 2nd revolution, the total torque provided by the turbine stabilizes on a steady value of 0.05105 with a maximum deviation from it equal to 0.51%. The value monitored in the simulation with rigid blades is equally steady (maximum deviation of 0.56%) and equal to 0.05243. Thus, the blade flexibility induces a drop of 2.6% in the torque provided by the turbine. Furthermore, when the torque contribution of a single blade is related to its azimuth angle, no remarkable difference (less than 0.75%) is observed between the behavior of the three blades in the second revolution. The same applies to any other quantity monitored on the blades, confirming that only one revolution is necessary to approach a periodic regime in time. Thus, one single blade is representative of the other two.

5.1. Effect of the deformations on the energy conversion

Despite the constancy of the total torque, the contribution of each blade is not constant over a full revolution and is largely affected by the ABL, as shown in fig. 10.

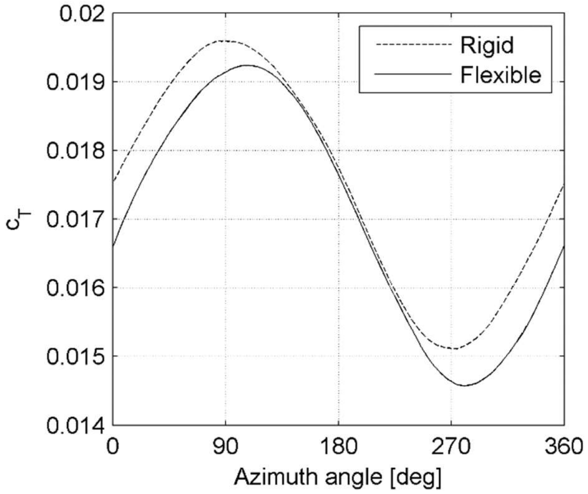

Fig. 10 – Single blade contribution to the torque.

When the blade points upwards (azimuth angle between 0° and 180°) the incoming wind velocity is larger and leads to larger angles of attacks on the entire blade span. On the other hand, when the blade points downwards (azimuth angle between 180° and 360°), the lower wind velocity decreases the angles of attack on the entire span, leading to a lower torque contribution. This is illustrated in Fig. 11 where the pressure contours around the same blade section (at 99% of the blade span) are shown for diametrically opposite azimuth angles.

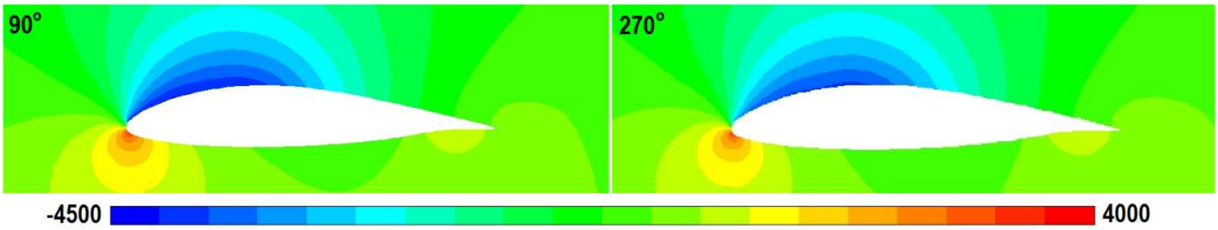

Fig. 11 –Pressure contours [Pa] around a blade section at 99% of the span for azimuth angles of 90° and 270°.

This perfectly applies to the simulation with rigid blades, where the maximum and minimum torque contribution for each blade is reached at azimuth angle of respectively 90° (i.e. blade vertically up) and 270° (i.e. blade vertically down). Differently, the torque contribution during the FSI simulation shows a delay (of about 20° azimuth angle) in both peaks, as well as a consistent negative offset with respect to the rigid simulation. In order to further investigate the origin of this difference, the blade is divided into 20 equally spaced strips, as shown in figure 12.

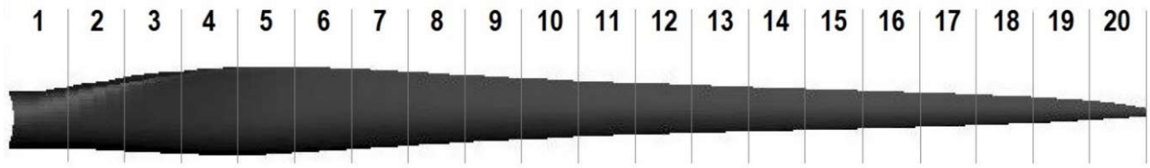

Fig. 12 – Blade strips.

The strips are defined and marked on the undeformed blade geometry and followed throughout its motion. Fig 13 shows the torque contribution of two different strips, one located approximately at half the blade span (strip 9) and one close to the tip (strip 19) for both rigid and flexible blade simulations.

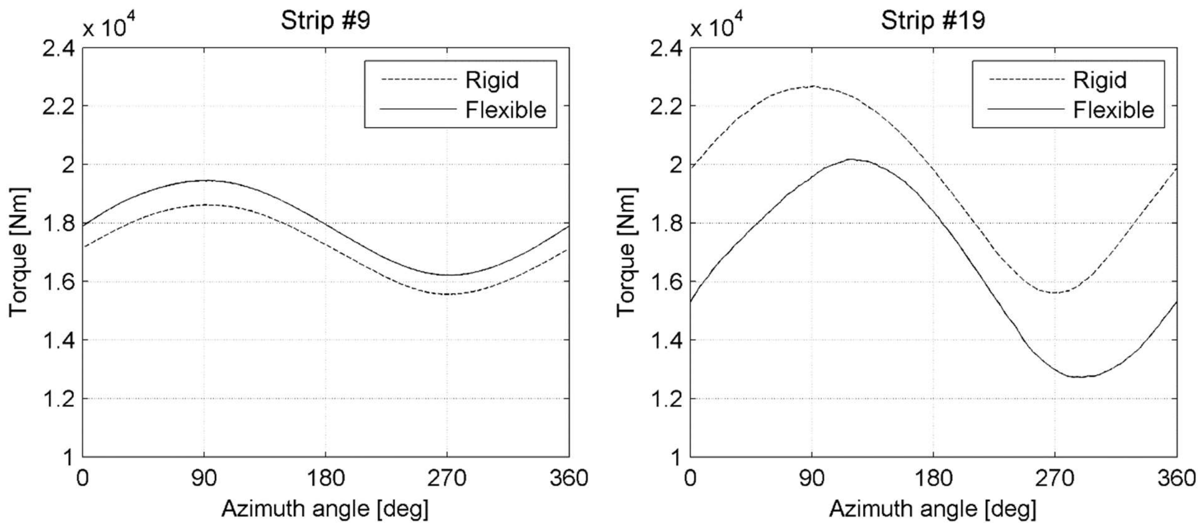

Fig. 13 – Torque contribution of two different blade strips: rigid and flexible blades.

The delay observed in the total torque contribution of a single blade in fig. 10 is thus not visible on the strips located far from the blade tip (as, for example, strip #9 in fig. 13) but it appears only in the strips located close to it (as shown for strip #19). This phenomenon can then be related directly to the axial and tangential oscillation of the tip, summarized in fig. 14.

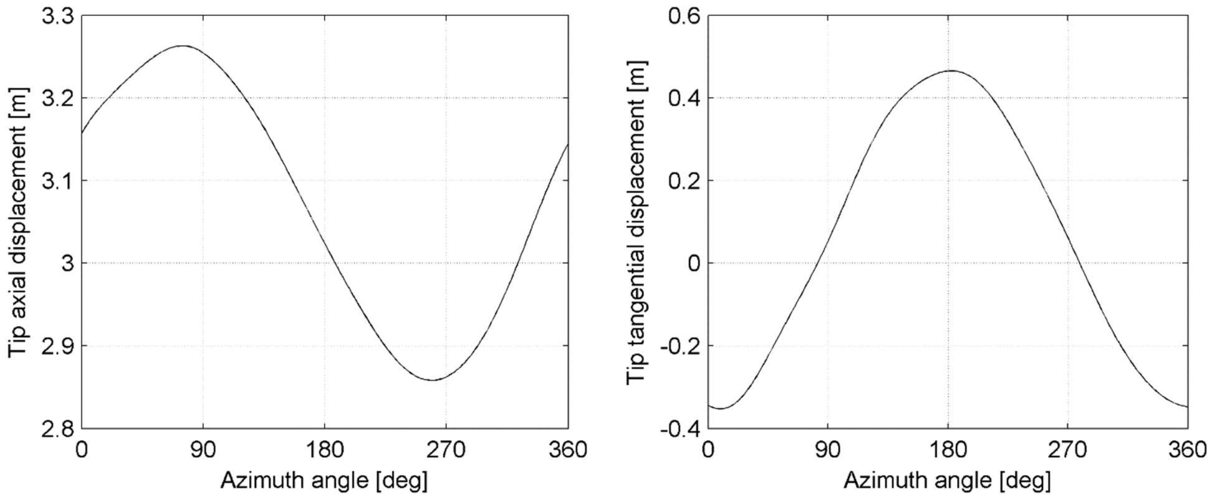

Fig. 14 – (left) axial and (right) tangential displacement of the blade tip.

The axial displacement fluctuates around an average value of about 3.1 m, corresponding to 6.2% of the blade span. Similar values are observed in other aeroelastic works carried out on turbines of similar sizes [3]. The axial displacement is always positive, indicating that the tip is always displaced backwards by the thrust exerted by the wind flow. Furthermore, fig. 15 shows the axial deformation (i.e. the biggest component of the total deformation) of the blade as a function of the span of the blade, in the moment of maximum (around 75° azimuth angle) and minimum (around 260° azimuth angle) axial displacement.

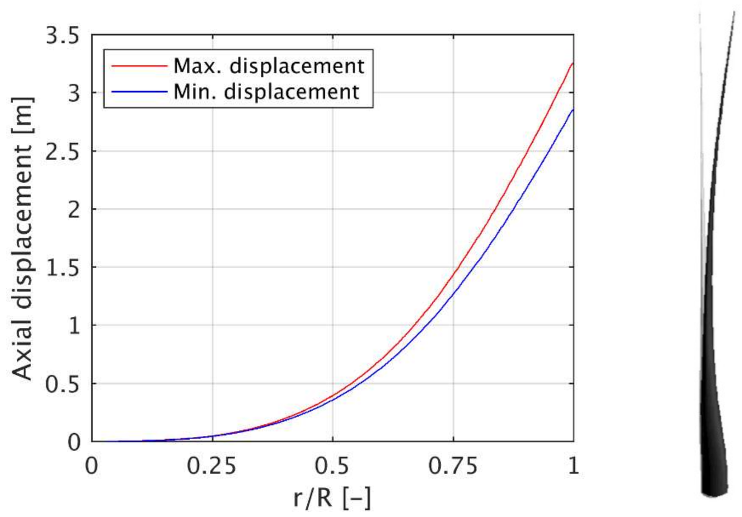

Fig. 15 – (left) axial displacement as a function of the blade span (where r/R is the relative radial position on the deformed geometry) at maximum and minimum displacement and (right) comparison between deformed and undeformed blade.

The oscillation of the blade tip, depicted in fig. 14, acts directly on the angle of attack of the relative flow. More in detail, when the tip axially moves towards the incoming wind (i.e. when its axial displacement decreases and its axial velocity is negative) the apparent wind velocity impacting on the blade increases, leading to a higher angle of the incoming flow on the tangential direction. On the other hand, when the blade tip tangentially moves in the direction of the blade rotation (i.e. when its tangential displacement increases and its tangential velocity is positive), the blade speed increases, leading to a lower angle. The axial and tangential velocities of the blade tip are obtained as time derivative of its axial and tangential displacements and are shown in fig. 16.

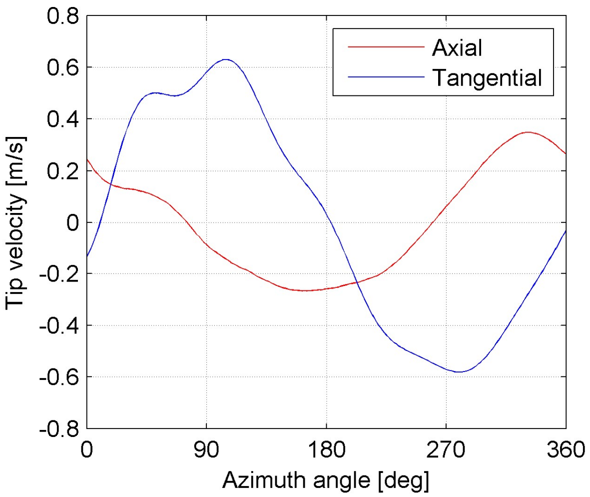

Fig. 16 – Axial and tangential velocity of the blade tip as a function of the azimuth angle.

These velocities can be combined with the varying incoming wind velocity of the ABL to calculate an approximate angle between the incoming relative velocity (deceleration due to the wind turbine not taken into account) and the tangential direction on the blade tip. Beside this, a non-zero deformation-induced twist angle is reported during the motion of each blade, as depicted in fig. 17, in addition to the twist of the rigid blade. The deformation-induced twist is considered positive if it tends to align the local chord of the blade airfoil with the incoming relative flow.

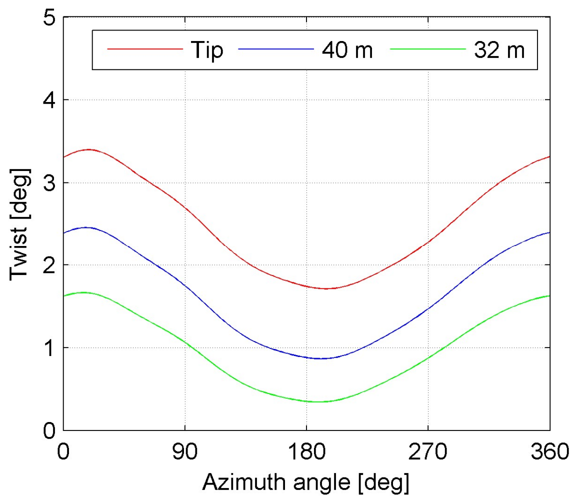

Fig. 17 – Deformation-induced twist of the blade at different spans, as a function of the blade azimuth angle.

Fig. 16 and 17 are combined to compute the approximate angle of attack (AoA, deceleration due to the wind turbine not taken into account) of the flow during the whole revolution. The difference (Flexible case – Rigid case) can then be computed for both the torque provided by strip #19 and the AoA around the tip section. Fig 18 is obtained by normalizing both these differences by the absolute value of their respective average and comparing them.

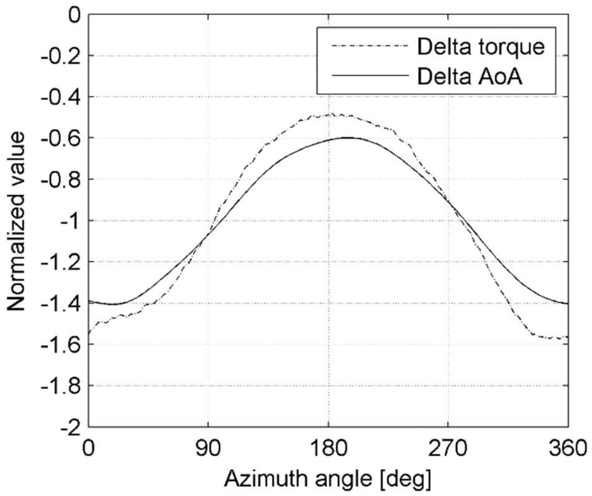

Fig. 18 – Normalized delta (Flexible case – Rigid case) in torque contribution of strip #19 and tip angle of attack.

Fig. 18 shows that both differences are always negative. Hence, a lower tip AoA corresponds to a loss in torque. Furthermore, peaks in the torque difference correspond in azimuth angle with peaks in the AoA difference, confirming that the blade deformation has a sensible impact on its performance and leads to both the delay and the phase shift observed in fig. 10. The upper part of the blade (i.e. the section closest to its tip) is most affected by the tip motion and, therefore, exhibits the largest difference in the provided torque.

Fig. 10 also shows a negative offset in the average value of the torque monitored in the flexible blade case. This negative offset is consistently reported during the whole revolution on strip #19. On the other hand, strip #9 shows a consistent (but small) gain in the torque. This condition is preserved throughout the entire revolution of the blade, as summarized by fig. 19 which shows the torque provided per meter of blade as a function of its span at two diametrically different azimuth angles.

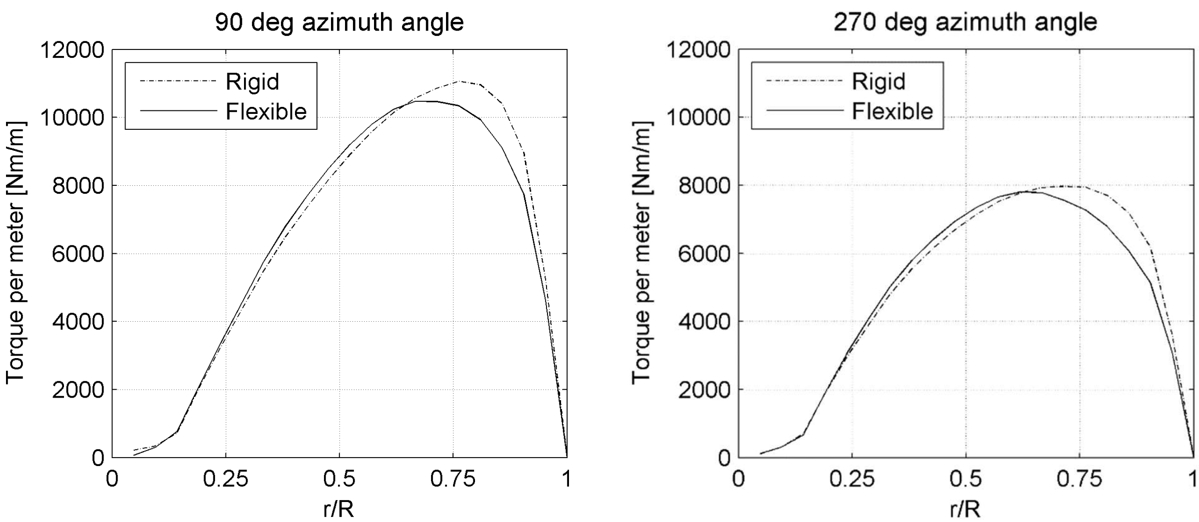

Fig. 19 – Torque per meter of blade as a function of the blade span at two diametrically opposite azimuth angles: (left) 90°, blade pointing vertically upwards and (right) 270°, blade pointing vertically downwards.

The area below each graph (i.e. the integral of each curve) in fig. 17 corresponds to the total torque provided by the blade. A consistent loss of efficiency is reported for the upper strips (#14 and beyond), while a small gain is reported for the lower ones. This results in a global lower efficiency of the blade when its flexibility is taken into account, as already displayed by fig. 10. This can be explained by the on average positive deformation-induced twist of the blade summarized by fig. 17.

5.2. Axial and radial wind loads

The total axial and radial wind forces acting on the blade are summarized in fig. 20. It is important to notice that both of them exhibit a negative feedback behavior: their average magnitude is increased in the deformed configuration with respect to the undeformed one. In particular, the average axial wind force is increased by approximately 6% and the axial displacement plotted in fig. 14 (left) follows the axial force in fig. 20 with a slight delay due to the inertia of the structure. On the other hand, the radial wind force, from centrifugal in the undeformed configuration, becomes consistently centripetal in the deformed configuration and its magnitude is roughly increased by 50%.

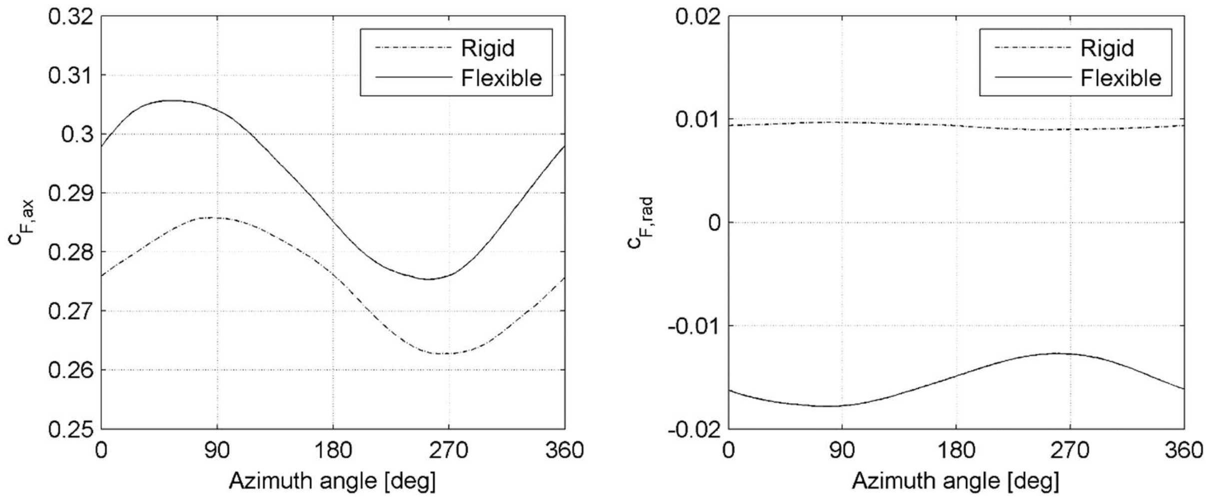

Fig. 20 – (left) axial and (right) radial integral forces on the blade.

Note that the centripetal force on the blade is a direct consequence of its deformed shape: the pressure difference between the pressure and the suction sides of the deflected blade will inevitably lead to such a force component (fig. 15 - right). This force is anyway negligible when compared to the total centrifugal force due to the blade rotation, as will be shown when analyzing the bending moment acting on the blade. This leads to a large safety margin with respect to possible buckling of the blade at this specific operating point.

5.3. Internal stresses and hub reaction forces

Focusing now on the internal stresses experienced by every flexible blade, the stress component S11 is computed aligned with the span-wise direction of the blades. The maximal stress (across the composite layup) distribution in both the outer shell and the inner webs is depicted in fig. 21 when the azimuth angle is 90°, namely the highest load condition.

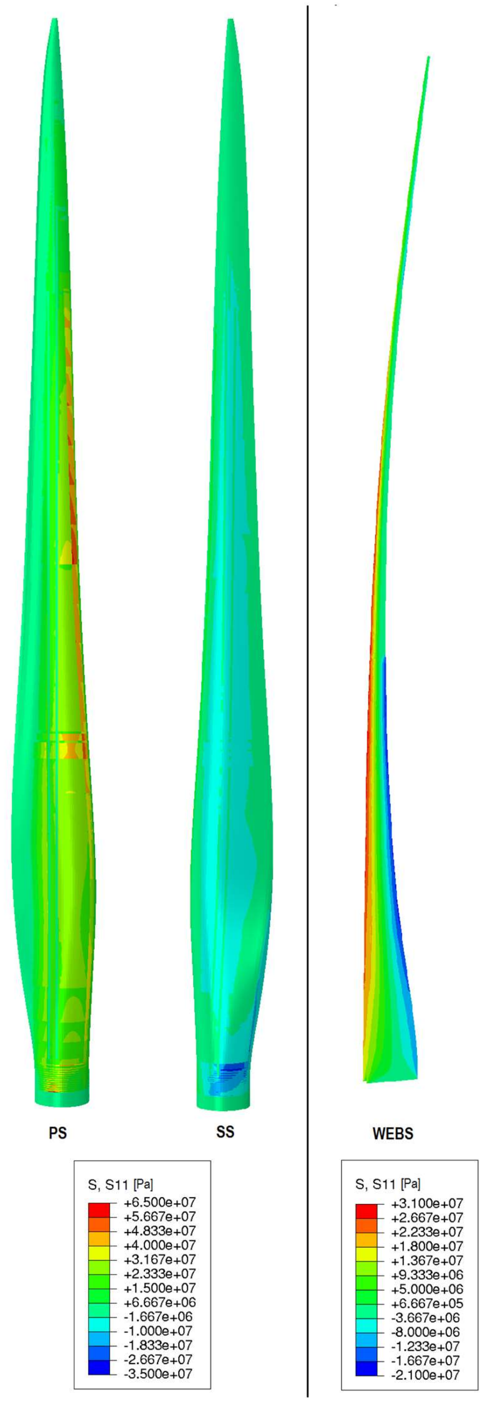

Fig. 21 – Longitudinal stresses [Pa] in the outer shell on the pressure side (PS), and suction side (SS) and in the shear webs at azimuth angle +90 ° during the simulation with flexible blades.

Notice that the longitudinal stress distribution follows from the bending solicitation acting on the blade: the pressure side experiences traction stress while the suction side is subject to a compression load. The stress in the points of maximal traction and maximal compression in the shear webs is shown in fig. 22:

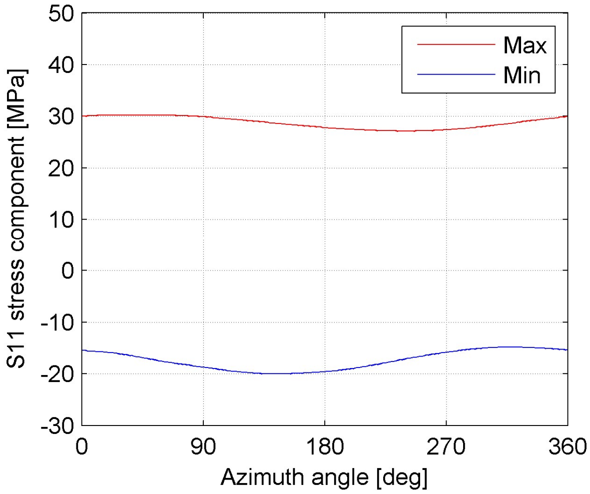

Fig. 22 – Stress evolution in the maximal traction and compression points of the shear webs.

Fig. 22 clearly shows the more intense flapwise bending solicitation in terms of gap between the maximal traction and the maximal compression when the blade approaches an azimuth angle around 90°. The flapwise bending moment will now be analyzed more in details as it represents the most intense solicitation acting on the structure. The axial tip displacement follows from this bending solicitation. The flapwise bending moment diagram of each blade is obtained considering the fluid forces (axial and radial), the centrifugal force induced by the blade rotation and the gravity force. Fig. 23 shows these diagrams at 2 different azimuth angles (90°, the highest load condition and 270°, the lowest load condition), displaying the total bending moment and the individual contributions of gravity, centrifugal force and radial force.

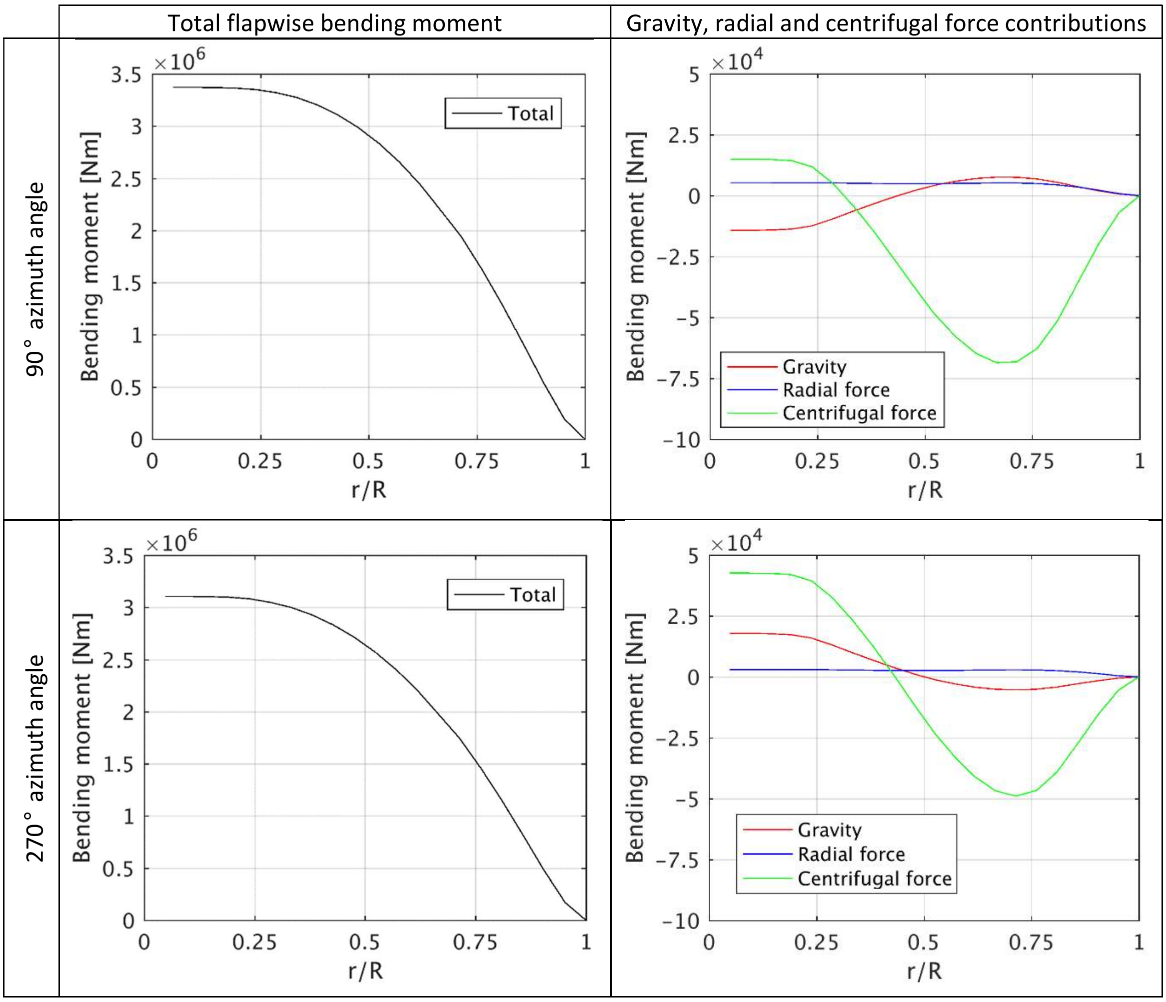

Fig. 23 – Flapwise bending moment diagrams: bending moment as a function of the radial position along the blade for azimuth angles of +90° (blade vertically up) and -90° (blade vertically down).

The main contribution to this bending moment comes always from the axial force acting on the blade. Also the centrifugal force sensibly contributes to reduce the bending moment acting on the blade. The contributions of radial fluid force and gravity force are respectively 3 and 2 orders of magnitude smaller than the axial force contribution. Nonetheless, the gravity force positively contributes to the bending moment in the upper section of the blade when it points upwards (at 90° azimuth angle). The opposite reasoning applies when the blade points downwards (at 270° azimuth angle) where the gravity force contributes to reduce the bending moment on the upper section of the blade. As anticipated, the radial force is negligibly small compared to the centrifugal one. Furthermore, the total bending moment diagrams are flat in the region closest to the root of the blade, indicating that this region gives a negligible contribution to the monitored bending moment. Nonetheless, monitoring the total bending reaction moment acting on the root of the 3 blades and computed by the structural solver, a mutual compensation of the three blades is visible, which leads to a total reaction moment about 1 order of magnitude lower than the individual one acting on the single blade, as shown in fig. 24.

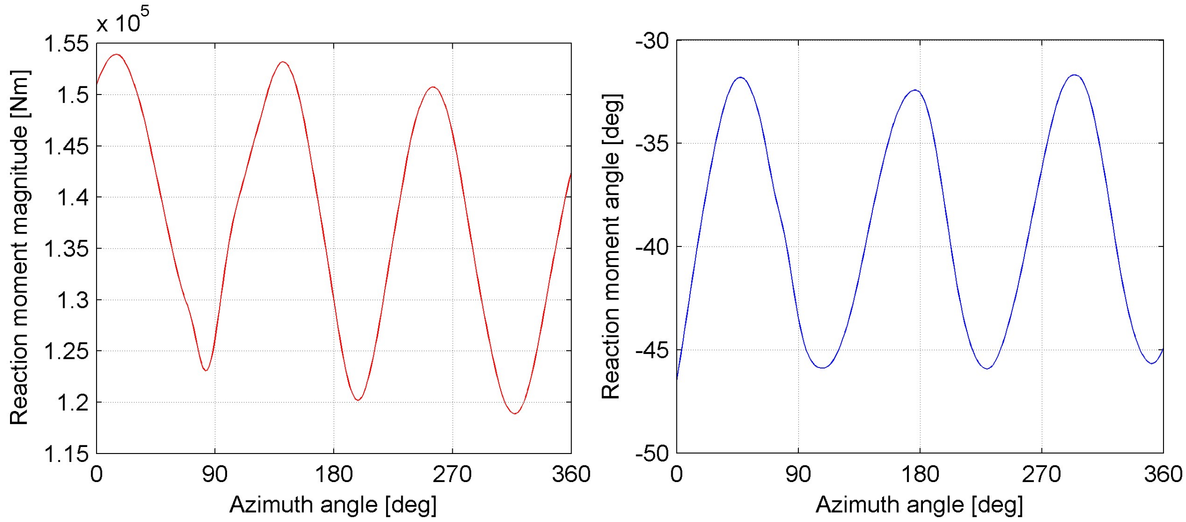

Fig. 24 – Total reaction moment on the root of the 3 blades: (left) magnitude and (right) azimuth angle of its direction as a function of the azimuth angle of one single blade.

The 3 peaks monitored in these quantities match with the blade passing frequency.

5.4. Effect of gravity

Finally, it is interesting to investigate the effect of the gravity loads on the results of the simulation with flexible blades. To this extent, the same setup is used, but the gravity load is excluded from the structural model (this is referred to as the "g-less" case). First, the behavior of the tip displacement is visibly affected by gravity, as summarized in fig. 25.

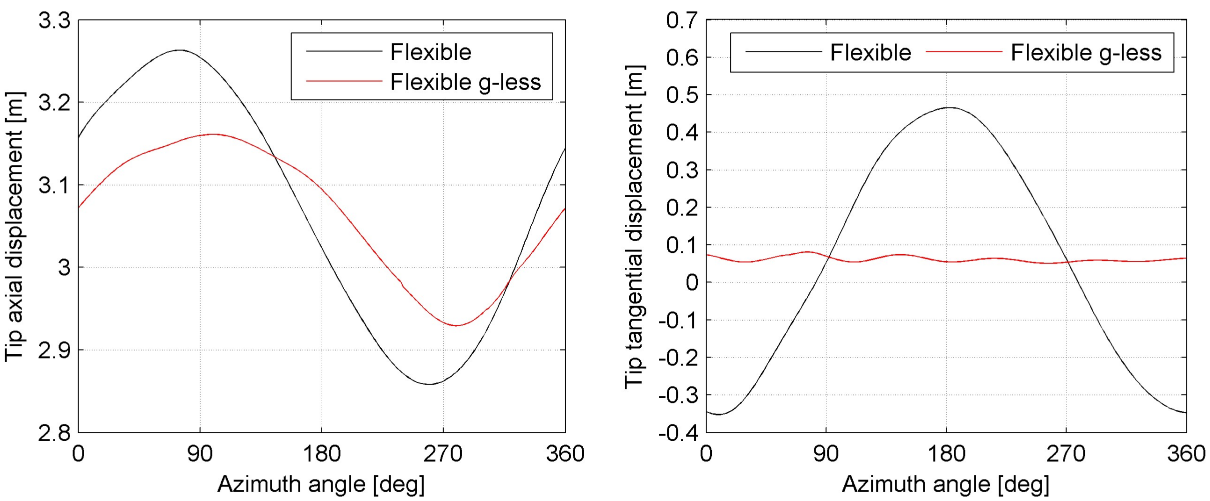

Fig. 25 – (left) axial and (right) tangential displacement of the blade tip with and without gravity load.

The gravity load largely affects the tangential tip displacement, especially when the blade is horizontally positioned (180° and 360° azimuth angles). On the other hand, when the blade is vertically positioned, the tangential displacements match in the two cases. It also tends to increase the axial displacement when the blade points upwards and reduce it when the blade points downwards, as already anticipated when examining the bending moment. Given the shift between the graphs reporting the axial displacement, the analysis of these graphs also points out the occurrence of some interaction between the two displacement components. The tangential velocity of the blade tip becomes negligible when gravity is neglected and, consequently, the delay in torque peaks and the oscillation amplitude of the torque addressed in fig. 10 are sensibly reduced, whereas the average value stays unchanged (fig. 26).

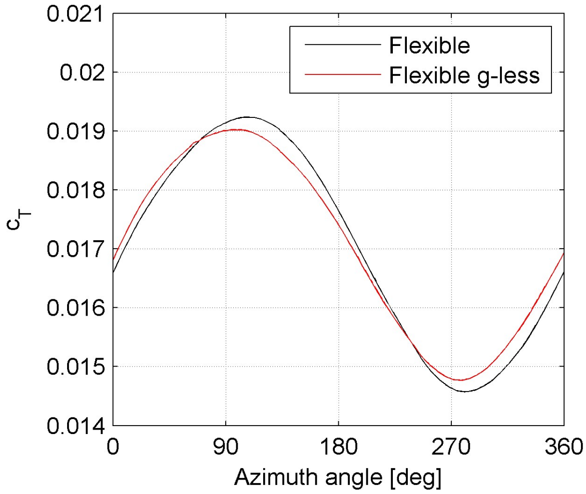

Fig. 26 – Single flexible blade contribution to the torque with and without gravity.

As a consequence, the torque distributions plotted in fig. 19 are not affected by the gravity load. Nevertheless, the same plots show remarkable differences when the blade is horizontally positioned, as confirmed by fig. 27.

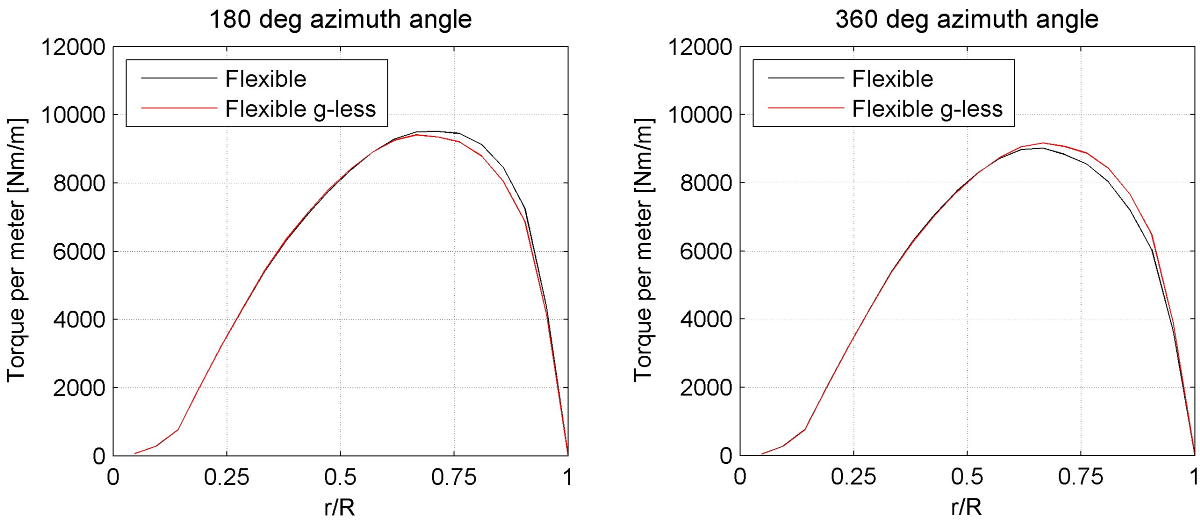

Fig. 27 – Torque per meter of blade as a function of the blade span at two diametrically opposite azimuth angles: (left) 180 ° , blade oriented horizontally right and (right) 360 °, blade oriented horizontally left.

Following the same reasoning already carried out about the influence of the blade tip velocity, the differences in the two graphs can be related to the different axial velocity (larger in magnitude when gravity is on), whereas the tangential velocity is, in both flexible and flexible g-less case, approximately zero.

6. CONCLUSIONS

A fully coupled FSI model of a 100 m diameter rotor was successfully created by combining a detailed structural model with a detailed fluid model. The structural model employs a refined mesh of shell elements positioned on the outer mold layer. The fluid model uses component meshes surrounding each blade and a background mesh, between which overset connectivity is built.

It was observed that the total torque is lower when FSI is considered. This results in a drop of efficiency of 6% for the single blade.

Unlike in prior literature, the ABL was included. It was observed that this has significant effect on the loads experienced by the blades. It is therefore advised to include the ABL in fluid simulations of wind turbines. While the total torque was found to remain relatively constant, the contribution of the individual blades was observed to vary with their rotational position. When including blade flexibility, it was observed that this variation lags (of about 20 ° azimuth angle) compared to the rigid case.

Furthermore, the torque contribution for different parts of the blade was investigated by creating blade strips. The delay in torque contribution was found to originate from the outboard part of the blade. For this reason, the oscillatory movement of the tip was analyzed. Both axial and tangential oscillation was observed. The average axial tip displacement corresponds to approximately 6% of the blade span and its oscillation is related to the presence of the ABL.

Furthermore, oscillating twisting deformation of the blade during each revolution was observed, with an average of 2.5 degrees of nose-down rotation. Based on these observations, the change in torque contribution is attributed to a change in AoA, due to a change in the tip speed and twist. This was shown to sensibly affect the torque distribution. The torque was found to decrease in the outboard region of the blade, while a small increase was observed towards the root.

Finally, the influence of gravity was investigated by running the same model, excluding gravitation loads from the structural side. Comparing the results with and without gravity, it was observed that this largely affects the tangential displacement of the tip. Consequently the tangential velocity became negligible, while the delay in torque contribution compared to the rigid case decreased. This proves that gravity has a significant influence and should be included. Furthermore, it reinforces the hypothesis that the delay in torque observed between the rigid and flexible cases respectively is the result of dynamic changes in AoA.

7. ACKNOWLEDGEMENTS

This work was supported by the Fonds Wetenschappelijk Onderzoek – Vlaanderen (FWO, grant no. G030414N). The computational resources (Stevin Supercomputer Infrastructure) and services used in this work were provided by the VSC (Flemish Supercomputer Center), funded by Ghent University, the Hercules Foundation and the Flemish Government department EWI.

8. APPENDIX

The ABL methodology outlined in section 2 and used in this work has been proposed by Parente et al. [14, 15], together with extensive validation work. Additional validation is presented here, where two test cases are built and described, together with their results. First, the stability of the imposed inlet profiles is tested in an empty 2D domain. Such a domain has a 200m high and 2000 m long rectangular shape. A structured mesh is built, with 70 cells in the vertical direction and 1200 cells in the longitudinal direction. The profiles for velocity, turbulent kinetic energy and turbulent dissipation rate are imposed at the inlet (choosing z_0 = 0.5m and u_*=1.38 m/s) and the modified wall functions are employed for the ground wall. The stability of the ABL profiles is checked by comparing them at the inlet and at the outlet, as shown in fig. A1:

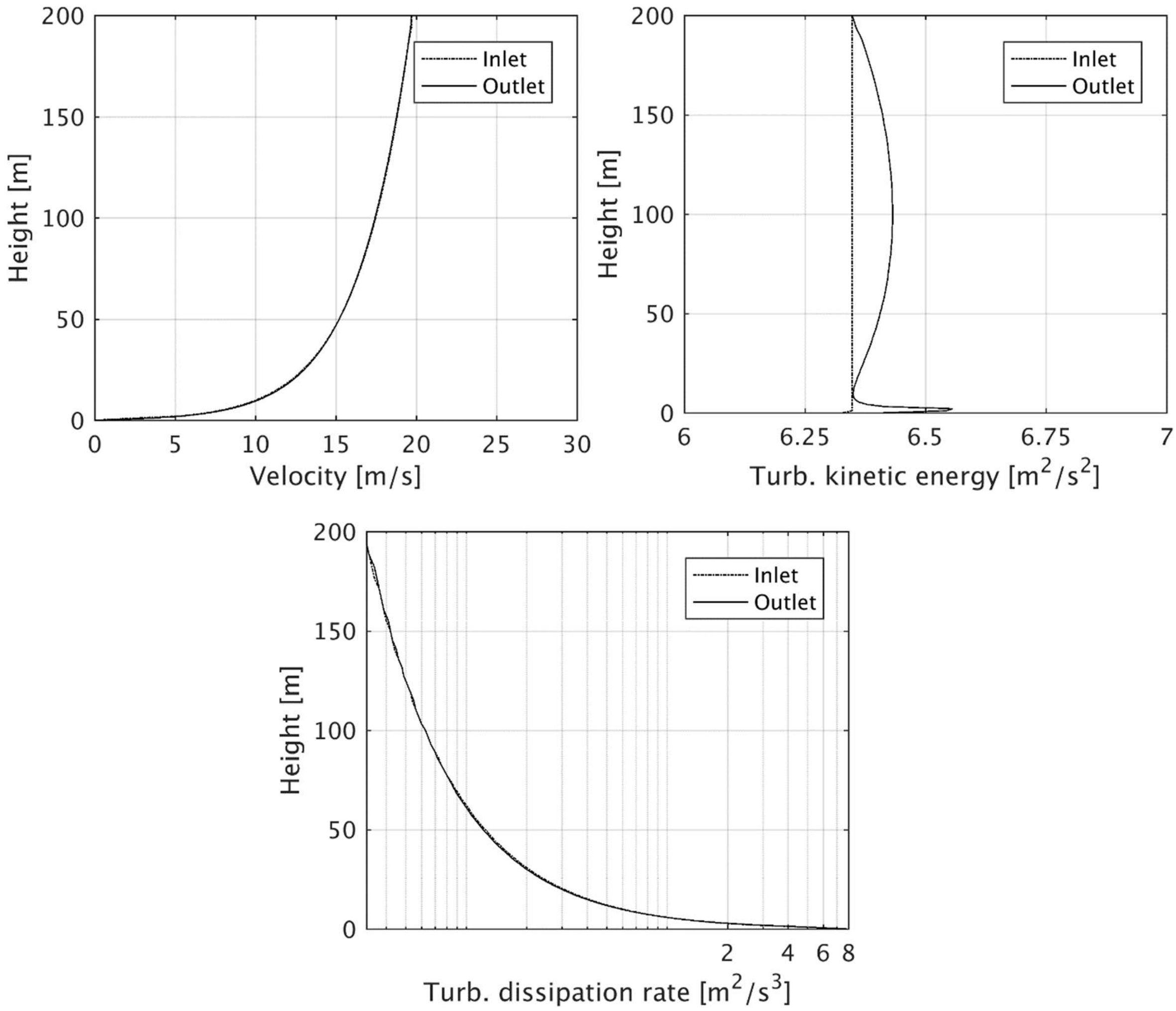

Fig. A1 – Stability of the ABL profiles in an empty 2D domain with modified wall functions.

Furthermore, the Silsoe cube experiment (described in [16]) is numerically reproduced. The Silsoe cube has edges of 6 m and is invested by an ABL flow aligned with it. The wind-induced pressure is monitored in several locations, along 3 different lines, each one cutting the cube in different directions (see figures 2 and 3). Modelling the experiment, just half of the cube has been reproduced, taking advantage of the geometrical symmetry. The resulting geometry is schematically shown in fig. A2:

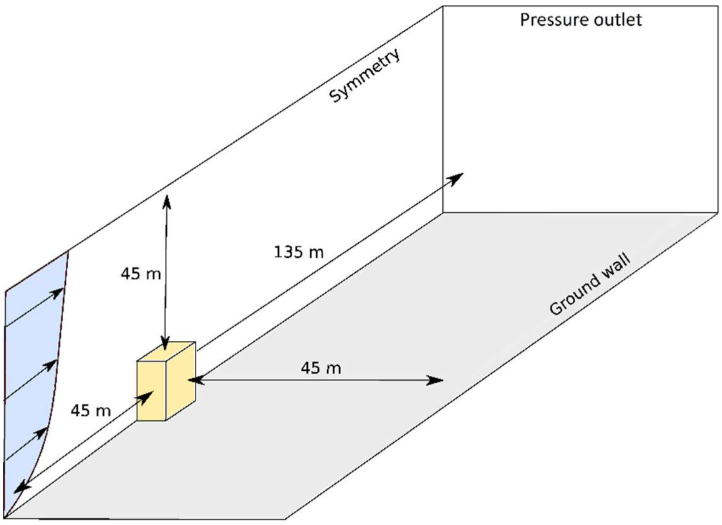

Fig. A2 – Silsoe cube simulation layout, with indication of the main dimensions and the boundary conditions.

The modified wall functions are employed on the ground wall (grey), while the standard ones are employed for the cube faces (yellow). The mesh is fully structured and consists of 8M cells. It is refined on the cube in order to guarantee values of the non-dimensional wall distance to always lay in the log layer. The comparison between experimental values and numerical predictions is reported in Fig. A3, together with the lines on which the values are monitored. The pressure coefficient c_p is computed as the static relative pressure divided by the dynamic pressure of the undisturbed flow.

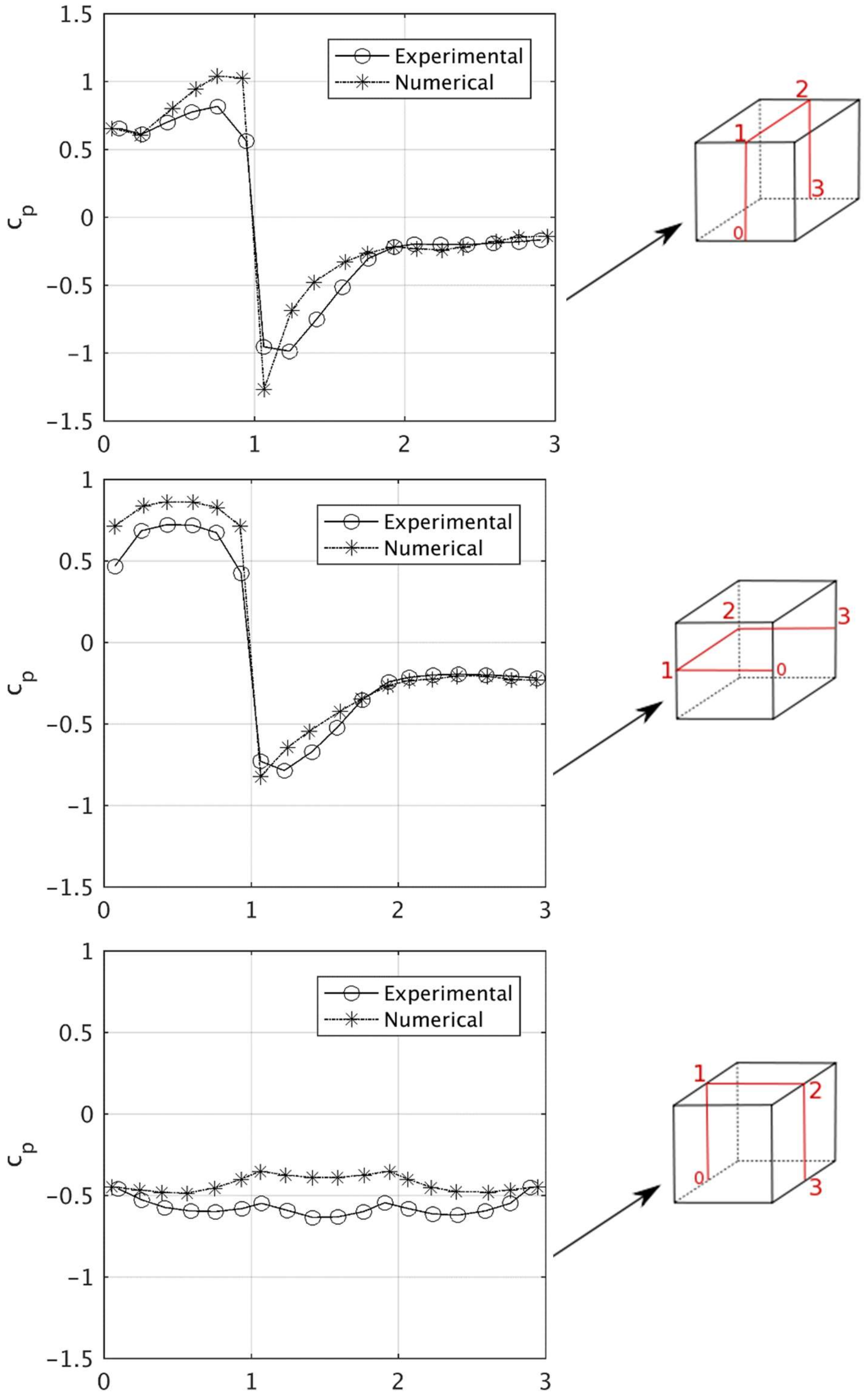

Fig. A3 – Numerical vs experimental comparison of wind-induced pressure on the Silsoe cube.

The agreement is satisfactory and the trend of the pressure distribution is always correctly predicted. The discrepancies seem to increase where separation occurs (e.g. point 1 in fig A3), confirming the usual tendency of most of the RANS models.

9. REFERENCES

1. M. Caduff, M.A.J. Huijbregts, H.J. Althaus, A. Koehler, S. Hellweg. Wind power electricity: the bigger the turbine, the greener the electricity? Environmental Science & Technology 2012. DOI: 10.1021/es204108n
2. Y. Bazilevs, M.C. Hsu, I. Akkerman, S. Wright, K. Takizawa, B. Henicke, T. Spielman, T.E. Tezduyar. 3D simulation of wind turbine rotors at full scale. Part I: Geometry modeling and Aerodynamics. International Journal for Numerical Methods in Fluids 2010. DOI: 10.1002/fld.2400
3. Y. Bazilevs, M.C. Hsu, I. Akkerman, S. Wright, K. Takizawa, B. Henicke, T. Spielman, T.E. Tezduyar. 3D simulation of wind turbine rotors at full scale. Part II: Fluid–structure interaction modeling with composite blades. International Journal for Numerical Methods in Fluids 2010. DOI: 10.1002/fld.2400
4. E. Hau. Wind Turbines: fundamentals, Technologies, Application, Economics (2nd Edition). Springer: Berlin, 2006.
5. D.W. MacPhee, A. Beyene. Fluid–structure interaction analysis of a morphing vertical axis wind turbine. Journal of Fluids and Structures 2016, ISSN 0889-9746.
6. H. Kim, S. Lee, E. Son. Aerodynamic noise analysis of large horizontal axis wind turbines considering fluid-structure interaction. Renewable Energy 2011, DOI: 10.1016/j.renene.2011.09.019.
7. YJ Lee, YT Jhan, CH Chung. Fluid–structure interaction of FRP wind turbine blades under aerodynamic effect. Composites Part B: Engineering 2012. ISSN 1359-8368.
8. J.C. Heinz, N.N. Sørensen, F. Zahle. Fluid–structure interaction computations for geometrically resolved rotor simulations using CFD. Wind Energy 2016. DOI: 10.1002/we.1976.
9. MC. Hsu, Y. Bazilevs. Fluid–structure interaction modeling of wind turbines: simulating the full machine. Computational Mechanics 2012. DOI: 10.1007/s00466-012-0772-0.
10. Y. Bazilevs, A. Korobenko, X. Deng, J. Yan. Novel structural modeling and mesh moving techniques for advanced fluid-structure interaction simulation of wind turbines. International Journal for Numerical Methods in Engineering 2015. DOI: 10.1002/nme.4738.
11. J. Degroote. Partitioned simulation of fluid-structure interaction: Coupling black-box solvers with quasi-Newton techniques. Archives of Computational Methods in Engineering, 20(3):185–238, 2013. DOI: 10.1007/s11831-013-9085-5.
12. P.J. Richards, R.P. Hoxey. Appropriate boundary conditions for computational wind engineering models using the k-ε turbulence model. Journal of Wind Engineering and Industrial Aerodynamics 1993, 46 & 47, 145-153.
13. Blocken B, Stathopoulos T, Carmeliet J (2007b) CFD simulation of the atmospheric boundary layer: wall function problems. Atmospheric Environment 41:238–252
14. A. Parente, C. Gorlé, J. van Beeck, C. Benocci. A Comprehensive Modelling Approach for the Neutral Atmospheric Boundary Layer: Consistent Inflow Conditions, Wall Function and Turbulence Model. Boundary Layer Meteorology 2011. DOI 10.1007/s10546-011-9621-5.
15. A. Parente, C. Gorlé, J. van Beeck, C. Benocci. Improved k–e model and wall function formulation for the RANS simulation of ABL flows. Journal of Wind Engineering and Industrial Aerodynamics 2011. DOI: 10.1016/j.jweia.2010.12.017.
16. P.J. Richards, R.P. Hoxey, J.L. Short. Wind pressures on a 6m cube. Journal of Wind Engineering and Industrial Aerodynamics. 2001. 89(14–15), 1553–1564.
17. M. Peeters , W. Van Paepegem. Development of automated high fidelity finite element models for large wind turbine blades. 16th European Conference on Composite Materials, Seville, Spain, 22-26 June 2014.
18. D.O. Yu, O.J. Kwon. Predicting wind turbine blade loads and aeroelastic response using a coupled CFD-CSD method. Renewable Energy 2014. DOI: 10.1016/j.renene.2014.03.033.

19. X. Liu, C. Lu, S. Liang, A. Godbole, Y. Chen. Vibration-induced aerodynamic loads on large horizontal axis wind turbine blades. Applied Energy 2016. DOI: 10.1016/j.apenergy.2015.11.080
20. A. Ahlström. Influence of wind turbine flexibility on loads and power production. Wind Energy 2006. DOI: 10.1002/we.167
21. M. Menon, F.L. Ponta. Dynamic aeroelastic behavior of wind turbine rotors in rapid pitch-control actions. Renewable Energy 2017. DOI: 10.1016/j.renene.2017.02.019
22. J. Franke, A. Hellsten, KH. Schlunzen, B. Carissimo. The COST 732 Best Practice Guideline for CFD simulation of flows in the urban environment: a summary. International Journal of Environment and Pollution, 2011. DOI: 10.1504/IJEP.2011.038443
23. L. Wang, R. Quant, A. Kolios. Fluid structure interaction modelling of horizontal-axis wind turbine blades based on CFD and FEA. Journal of Wind Engineering and Industrial Aerodynamics, 2016. DOI: 10.1016/j.jweia.2016.09.006
24. M. Sayed, Th. Lutz, E. Krämer, Sh. Shayegan, A. Ghantasala, R. Wüchner, K.-U. Bletzinger. High fidelity CFD-CSD aeroelastic analysis of slender bladed horizontal-axis wind turbine. Journal of Physics: Conference Series, 2016. DOI: 10.1088/1742-6596/753/4/042009
25. I.F.S. Ahmed Kabir, E.Y.K. Ng. Effect of different atmospheric boundary layers on the wake characteristics of NREL phase VI wind turbine. Renewable Energy, 2019. DOI: 10.1016/j.renene.2018.08.083
26. J. Wieringa. Updating the Davenport roughness classification. Journal of Wind Engineering and Industrial Aerodynamics, 1992. DOI: 10.1016/0167-6105(92)90434-C
27. S. Sicklinger, C. Lerch, R. Wüchner, K-U. Bletzinger. Fully coupled co-simulation of a wind turbine emergency brake maneuver. Journal of Wind Engineering and Industrial Aerodynamics, 2015. DOI: 10.1016/j.jweia.2015.03.021